AGU100 ADVANCING EARTH AND SPACE SCIENCE

Water Resources Research

RESEARCH ARTICLE
10.1002/2017WR021360

Key Points:
- The technique described in this paper is useful for visualization and efficient inversion
- The trajectory-based approach is valid for an arbitrary porous medium

Correspondence to:
D. W. Vasco,
dwvasco@lbl.gov

Citation:
Vasco, D. W. (2018). An extended trajectory mechanics approach for calculating the path of a pressure transient: Derivation and illustration. *Water Resources Research*, *54*. https://doi.org/10.1002/2017WR021360

Received 21 JUN 2017
Accepted 12 MAR 2018
Accepted article online 25 MAR 2018

An Extended Trajectory Mechanics Approach for Calculating the Path of a Pressure Transient: Derivation and Illustration

D. W. Vasco[1]

[1]Lawrence Berkeley National Laboratory, University of California, Berkeley, Berkeley, CA, USA

Abstract Following an approach used in quantum dynamics, an exponential representation of the hydraulic head transforms the diffusion equation governing pressure propagation into an equivalent set of ordinary differential equations. Using a reservoir simulator to determine one set of dependent variables leaves a reduced set of equations for the path of a pressure transient. Unlike the current approach for computing the path of a transient, based on a high-frequency asymptotic solution, the trajectories resulting from this new formulation are valid for arbitrary spatial variations in aquifer properties. For a medium containing interfaces and layers with sharp boundaries, the trajectory mechanics approach produces paths that are compatible with travel time fields produced by a numerical simulator, while the asymptotic solution produces paths that bend too strongly into high permeability regions. The breakdown of the conventional asymptotic solution, due to the presence of sharp boundaries, has implications for model parameter sensitivity calculations and the solution of the inverse problem. For example, near an abrupt boundary, trajectories based on the asymptotic approach deviate significantly from regions of high sensitivity observed in numerical computations. In contrast, paths based on the new trajectory mechanics approach coincide with regions of maximum sensitivity to permeability changes.

Plain Language Summary I present a new approach for computing the path of a pressure transient in a highly heterogeneous porous medium. The approach utilizes methods developed in quantum dynamics. The trajectories are useful for visualizing pressure propagation in complicated physical models and may form the basis for an efficient tomographic imaging algorithm.

1. Introduction

The use of transient pressure and hydraulic head data to infer aquifer properties has a long and varied history (Bohling et al., 2002; Brauchler et al., 2003, 2010; Butler et al., 1999, 2003; Cardiff & Barrash, 2011; Cardiff et al., 2013a, 2013b; Carrera & Neuman, 1986; He et al., 2006; Hsieh et al., 1985; Hu et al., 2011; Jacquard & Jain, 1965; Karasaki et al., 2000; Oliver, 1993; Paillet, 1993; Vasco et al., 2000; Vasco & Karasaki, 2001; Yeh et al., 2008; Yeh & Liu, 2000). One advantage of approaches based on pressure and hydraulic head is the rapid propagation of pressure transients in comparison to methods such as tracer transport and multiphase flow, leading to faster experiments and better turn-around times. Developments in experimental techniques, such as crosswell slug tests and multiwell tomography, are providing ever larger sets of pressure and hydraulic head observations for the imaging of flow properties. Technological advances, including fiber optic cables, downhole pressure sensors, and slim hole drilling, may lead to the expansion of transient pressure testing and time-lapse monitoring.

While one may use the full pressure or hydraulic head waveform in the interpretation of transient tests, there are certain advantages associated with the use of the travel times of a transient disturbance. The arrival of a pressure transient at an observation borehole typically occurs well before a steady state is attained, greatly reducing the time required for an experiment. The interpretation of a travel time, particularly for the high-frequency component of a pressure transient, is relatively straight forward in comparison to the interpretation of its amplitude (Vasco, 2008; Vasco et al., 2000). Furthermore, it is possible to interpret pressure-related geophysical observations, such as tiltmeter and Interferometric Synthetic Aperture Radar (InSAR) data, in terms of transient pressure propagation, based on the concept of an onset time (Rucci et al., 2010; Vasco, 2004; Vasco & Datta-Gupta, 2016; Vasco et al., 2014). Such an approach is primarily sensitive to

the flow properties of the medium and not sensitive to the rock physics model used to describe the coupling (Rucci et al., 2010; Vasco et al., 2014). As in elastic wave propagation, it has been shown that the inverse problem for travel times is quasi-linear while that for amplitudes is strongly nonlinear (Cheng et al., 2005). Therefore, the solution of a travel time inverse problem is much less sensitive to the starting or initial model. Treating a single arrival time, rather than the entire transient pressure waveform, provides a significant reduction in computational complexity and leads to efficient inversion algorithms. This is particularly advantageous in a crosswell or multiwell setting. Taken together, these factors suggest that transient pressure travel time inversion provides a robust and efficient approach for constructing an initial image of flow properties, such as hydraulic diffusivity.

A useful formulation of transient pressure propagation is based on a high-frequency asymptotic solution of the diffusion equation (Cohen & Lewis, 1967; Vasco et al., 2000; Virieux et al., 1994). The notion of what constitutes a high frequency is referenced to the spatial variation of the corresponding pressure transient and its length scale in comparison with the shortest length scale of the heterogeneity of the medium. In fact, we can frame the asymptotic approach in terms of the ratio of these two length scales, denoted by ε (Vasco & Datta-Gupta, 2016). The approximate solution is a power series in this ratio, and when ε is small only the first one or two terms of the power series are significant. In this framework, the modeling is partitioned into a nonlinear differential equation associated with the propagation time or phase, the eikonal equation, and a transport equation describing the evolution of the amplitude. Efficient numerical techniques for the solution of the eikonal equation, such as the Fast Marching method, can be used to compute travel times for large forward problems (Fujita et al., 2015; Zhang et al., 2014). A high-frequency solution may be defined along trajectories that are the bicharacteristics of the eikonal equation (Chapman, 2004; Luneburg, 1966; Kline & Kay, 1965). The trajectory-based solution leads to imaging algorithms that are akin to medical and geophysical tomography (Brauchler et al., 2003; Vasco, 2008; Vasco et al., 2000). However, the high-frequency asymptotic solution is based on rather severe assumptions that break down in the presence of layering and fractures. Specifically, it is assumed that either the frequencies contained in the transient disturbance are so high, or that the properties of the medium vary so smoothly, that the length scale across the front of the transient disturbance is much less than the length scale of any heterogeneity in the medium. A sharp interface can be included explicitly as a boundary condition, producing the equivalent of snell's law of refraction (Chapman, 2004). However, when solving the inverse problem one does not typically know the location and nature of all internal boundaries a priori.

It would be useful to have a generally valid approach that retains much of the efficiency of the high-frequency asymptotic approach. In the work that follows, we present a trajectory-based technique for modeling pressure propagation and travel times, making no assumptions regarding the smoothness of the medium or regarding the magnitude of the variations in its properties. To be clear, we will require the regularity necessary for the validity of the partial differential equation governing fluid flow, such as a piecewise continuous medium. The technique is an adaptation of a method from quantum mechanics that is used as a visualization and computational tool for studying larger chemical systems (Garashchuk, 2010; Garashchuk et al., 2011; Garashchuk & Vazhappilly, 2010; Goldfarb et al., 2006; Liu & Makri, 2005; Wyatt, 2005). The implementation in quantum mechanics requires the solution of two coupled nonlinear partial differential equations, extended forms of the eikonal and transport equations. However, in our formulation, we take advantage of existing reservoir simulators to solve for one of the variables in the coupled system. The outcome is a single ordinary differential equation for the trajectory, $\mathbf{x}(t)$, describing the path of a propagating disturbance as a function of time t. Such trajectories provide insight into the nature of pressure propagation in a medium containing abrupt layers and boundaries. We illustrate the approach using several examples involving increasingly sharp boundaries.

2. Methodology

2.1. The Governing Equations for Hydraulic Head

Our starting point is the equation governing the evolution of hydraulid head $h(\mathbf{x}, t)$ in both space $\mathbf{x}=(x, y, z)$ and time t in a porous medium. The conservation of mass, in conjunction with Darcy's law, provides the governing equation. We will adopt the version presented in de Marsily (1986, p. 109):

$$\nabla \cdot (\mathbf{K} \cdot \nabla h) = \zeta \frac{\partial h}{\partial t}, \tag{1}$$

where $\mathbf{K}$ is the hydraulic conductivity, a symmetric tensor, and ζ is the specific storage coefficient given by

$$\zeta = \rho \varphi g \left(\beta_l + \beta_s + \frac{\alpha}{\varphi} \right). \tag{2}$$

In this expression, ρ is the fluid density, φ is the total porosity of the medium, g is the gravitational acceleration, β_l is isothermal compressibility of the liquid, β_s is the compressibility of the solid constituents, and α is the compressibility of the porous matrix. For an incompressible fluid, the pressure is related to the hydraulic head according to

$$p(\mathbf{x}, t) = \rho g h(\mathbf{x}, t) - z, \tag{3}$$

where z is the height above a reference location.

2.2. An Equation for the Trajectories Associated With Transient Fluid Flow

As stated above, our goal is to introduce trajectories that may be used to visualize transient fluid flow and to develop efficient crosswell tomographic algorithms for imaging flow properties. The trajectory may be thought of as the path of a transient disturbance due to an impulsive pressure source, or, as shown in Vasco et al. (2000), as the path of the most rapidly varying component of pressure or head, when the source is a step function. We will denote the trajectory by $\mathbf{x}(t)$ where the position along the path depends on time. Unlike the high-frequency asymptotic expressions developed previously for both trajectory and front calculations (Brauchler et al., 2003, 2011; Fujita et al., 2015; He et al., 2006; Vasco, 2008; Vasco & Datta-Gupta, 2016; Vasco et al., 2000; Zhang et al., 2014), our expressions for the trajectories will be valid under very general conditions and for arbitrary distributions of $\mathbf{K}(\mathbf{x})$ and $\zeta(\mathbf{x})$.

An expression for the trajectory associated with the propagation of a transient fluid front follows from substituting the representation:

$$h(\mathbf{x}, t) = e^{-S(\mathbf{x}, t)} \tag{4}$$

into the governing equation (1) for hydraulic head. Here we outline the approach, providing the details of of the derivation in Appendix A. The resulting equation for $S(\mathbf{x}, t)$, known as the phase, may be written as

$$\frac{\partial S}{\partial t} + \mathbf{v} \cdot \nabla S = \frac{1}{\zeta} \nabla \cdot (\mathbf{K} \cdot \mathbf{p}), \tag{5}$$

where $\mathbf{v}$ is a velocity, given by

$$\mathbf{v} = \mathbf{p} \cdot \frac{\mathbf{K}}{\zeta}, \tag{6}$$

and $\mathbf{p}$ is the spatial gradient of the phase:

$$\mathbf{p} = \nabla S. \tag{7}$$

We can solve equation (4) for $S(\mathbf{x}, t)$ and apply the gradient to arrive at an expression for $\mathbf{p}$ in terms of $h(\mathbf{x}, t)$,

$$\mathbf{p} = -\nabla \ln h. \tag{8}$$

Now consider equation (5) in a moving coordinate system, in which the tangent vector of the coordinate curves is denoted by $\mathbf{v}$. Parameterize the position along each coordinate curve, $\mathbf{x}(t)$, by the time t, and therefore equation (5) becomes

$$\frac{dS}{dt} = \frac{\partial S}{\partial t} + \frac{d\mathbf{x}}{dt} \cdot \nabla S = \frac{1}{\zeta} \nabla \cdot (\mathbf{K} \cdot \mathbf{p}). \tag{9}$$

Because $\mathbf{v}$ is the tangent vector to the path $\mathbf{x}(t)$, we can equate it to $d\mathbf{x}/dt$ and use equations (6) and (8) to produce a differential equation for the trajectory,

$$\frac{d\mathbf{x}}{dt} = \mathbf{v} = -\frac{\mathbf{K}}{\zeta} \cdot \nabla \ln h. \tag{10}$$

Equation (10) also follows from an application of the method of characteristics to the scalar differential equation (5) (Courant & Hilbert, 1962). Equation (10) clearly lays out the contributions of $h(\mathbf{x},t)$, $\mathbf{K}(\mathbf{x})$, and $\zeta(\mathbf{x})$ to the trajectories. Note that, due to the presence of the logarithm, the sensitivity of the trajectories to lateral variations of the hydraulic head is somewhat muted.

Ultimately, equation (10) will provide our fundamental expression for computing trajectories. However, as a stand-alone equation, it is incomplete because we do not know $h(\mathbf{x},t)$. One could derive a complete set of equations by combining equations (6) and (10) to form the first set of defining equations. The second set of equations follows from applying the gradient operator to both sides of equation (9) and noting the definition of the slowness or phase gradient vector $\mathbf{p}$ given by equation (7). The resulting system of coupled ordinary differential equations for $\mathbf{x}$ and $\mathbf{p}$ takes the form:

$$\frac{d\mathbf{x}}{dt} = \frac{1}{\zeta}\mathbf{p}\cdot\mathbf{K}, \tag{11}$$

$$\frac{d\mathbf{p}}{dt} = \nabla\left[\frac{1}{\zeta}\nabla\cdot(\mathbf{K}\cdot\mathbf{p})\right]. \tag{12}$$

We could solve equations (11) and (12) using numerical techniques for integrating ordinary differential equations (Press et al., 1992). This is the approach most commonly adopted in quantum dynamics when using trajectory-based methods to solve for the evolution of many particle systems (Garashchuk et al., 2011; Garashchuk & Vazhappilly, 2010; Wyatt, 2005). The presence of the gradient operator in equation (12) complicates the numerical approach and links adjacent trajectories, necessitating coupled calculations of the field $(S\mathbf{x},t)$ and the paths. Still the approach is quite efficient and requires less time then fully numerical, grid-based solutions of the diffusion-like equations encountered in quantum mechanics, forming the basis for the treatment of complicated chemical systems (Wyatt, 2005).

Here we adopt an alternative approach in solving for the trajectories, taking advantage of the sophisticated numerical simulators for modeling fluid flow and transport. Specifically, we utilize a simulator, such as TOUGH2 (Pruess et al., 1999) to determine $h(\mathbf{x},t)$, and integrate equation (10) directly to find the path $\mathbf{x}(t)$. The ordinary differential equation (10) can be solved directly and simply using a numerical technique such as a Runge-Kutta method (Cash & Karp, 1990; Press et al., 1992, p. 704). Because the field $h(\mathbf{x},t)$ is known from the reservoir simulation, one simply marches up the field in the direction of the head gradient from the observation point to the source of the transient disturbance.

In order to gain some insight into the nature of the propagation of a pressure or head transient, let us consider the expression (10) in greater detail. The coefficient $\mathbf{K}/\zeta$ is the diffusivity, with units of L^2/T, a quantity related to the propagation of pressure in a porous medium. On first sight, equation (10) appears to lack the correct dimensionality (units), but if we apply the gradient operator to the logarithm we arrive at

$$\frac{d\mathbf{x}}{dt} = -\frac{\mathbf{K}}{\zeta}\cdot\frac{\nabla h}{h}, \tag{13}$$

which has units of velocity [L/T] because the gradient operator introduces a factor with dimensions of $1/L$. The factor containing $h(\mathbf{x},t)$ results in a time-dependent propagation velocity. When considered in the frequency domain, after applying the Fourier transform, this produces a frequency-dependent velocity, leading to dispersion. Dispersive propagation is characteristic of diffusive processes such as the evolution of a pressure front, as illustrated in Figures 1 and 2. In Figure 1, the time derivatives of the pressure variation in each grid block of a numerical simulation are plotted. The pressure derivatives are normalized by the peak magnitude obtained in the grid block, to account for the decay of the pressure with distance from the source. The simulation corresponds to injection in a small interval of a borehole, with a step-like rate change. The outward propagation of the pressure disturbance is clear in this figure. The medium is characterized by an abrupt jump in permeability at an elevation of 7.5 m. The permeability increases with depth by almost an order of magnitude. The dispersion is evident as a broadening of the disturbance as it propagates away from the source. The toe of the front appears to advance rapidly, particularly in the high permeability half-space. The dispersion is clearly visible in the time series of pressure and pressure derivatives for three locations within the grid (Figure 2). The observations points are at the same elevation (5.1 m) as the source but at increasing distances. The form of the propagating disturbance changes dramatically as it

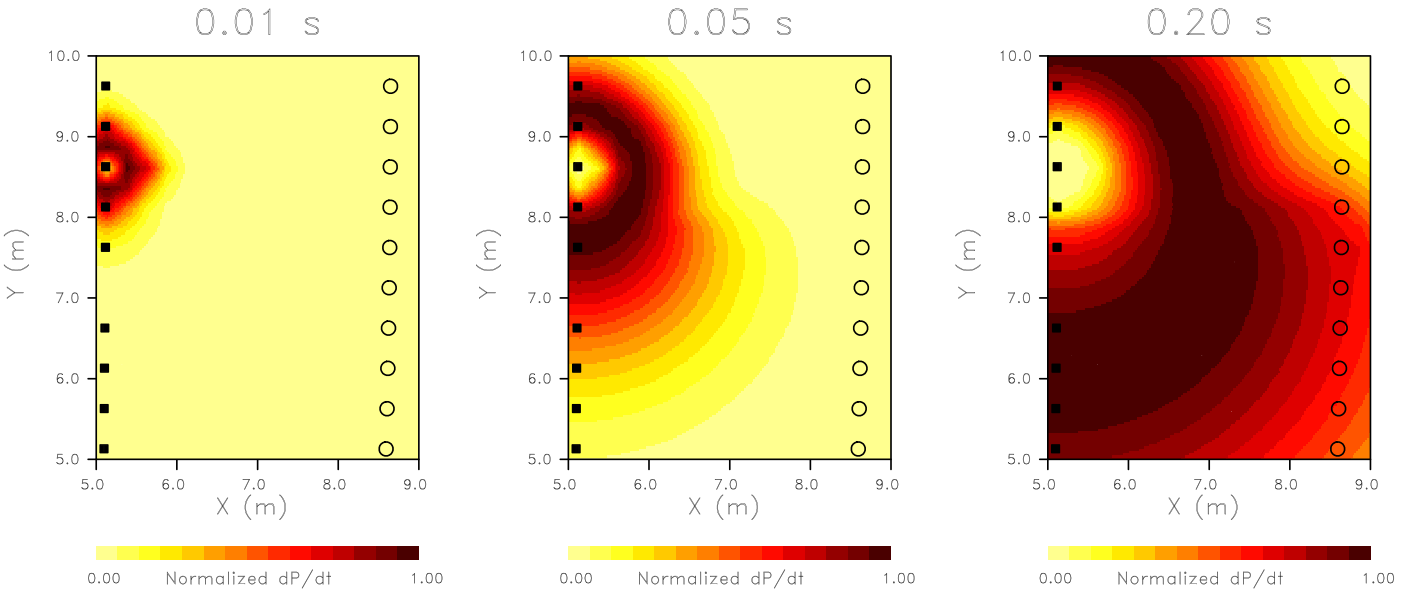

Figure 1. Normalized time derivatives of the transient pressure variation due to a step-like injection at the point (5.2, 8.6 m). Three snapshots are plotted, corresponding to 0.01, 0.05, and 0.20 s after the start of injection. The derivatives are normalized to unit peak amplitude by dividing by the largest derivative magnitude obtained in each grid block.

moves away from the source. In Figure 3, we plot the trajectories, obtained from an integration of equation (10), for propagation from the source to 10 observation points. The trajectories are displayed along with the logarithm of the pressure field variation calculated to have occurred 6.0 s after the start of injection. The influence of the permeability change on the pressure field is evident in the change in spacing of the pressure contours near 7.5 m. The propagation paths bend due to presence of the higher permeability half-space at depth and its effect on the head or pressure field, as indicated by equations (10) and (13).

2.3. A Comparison With a High-Frequency Asymptotic Approach and the Eikonal Equation

Previous calculations of trajectories and pressure fronts invoked a high-frequency asymptotic argument (Brauchler et al., 2003; Fujita et al., 2015; Vasco, 2008; Vasco et al., 2000). In this section, we compare the equations for the trajectories that result from the asymptotic approach to the trajectory mechanics expression (10). Though it would take us too far afield to reproduce the derivation of the high-frequency solution, we can arrive at some results fairly quickly by starting with equation (5) and substituting in for the variables **v** and **p** using equations (6) and (7), respectively,

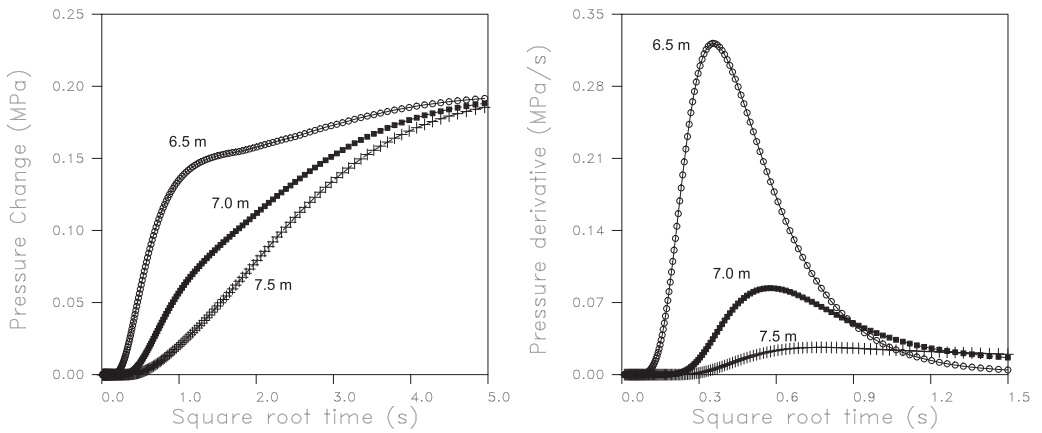

Figure 2. Pressure changes and pressure derivatives as a function of time for three points at various distances from the injection point. The curves are labeled by the distance from the pressure source.

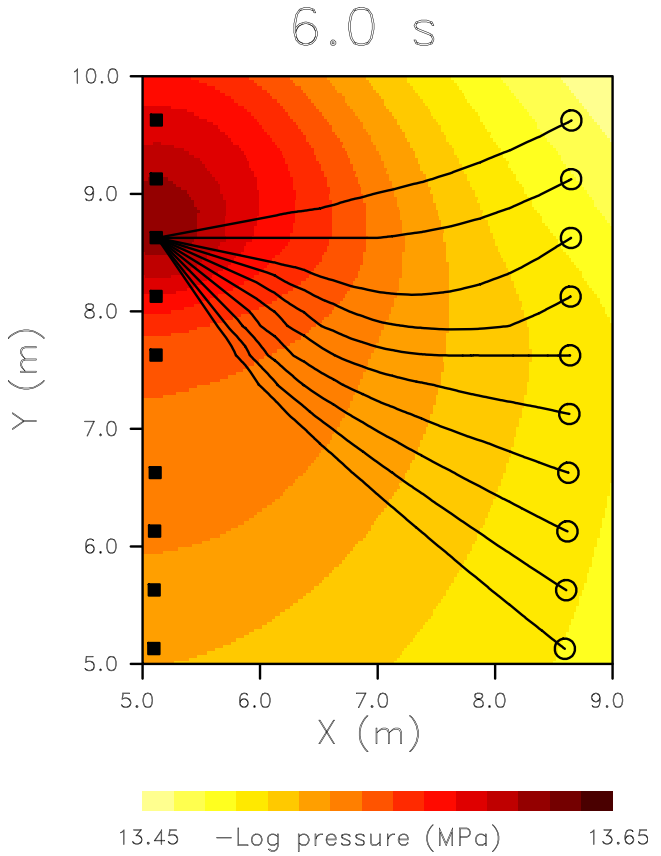

Figure 3. Trajectories associated with the propagation of pressure disturbances from a source on the left to 10 receivers on the right. The color field indicates the negative logarithm of the pressure variation 6 s after the start of injection, calculated using the TOUGH2 numerical simulator (Pruess et al., 1999).

$$\frac{\partial S}{\partial t}+\nabla S\cdot\frac{\mathbf{K}}{\zeta}\cdot\nabla S=\frac{1}{\zeta}\nabla\cdot(\mathbf{K}\cdot\nabla S). \tag{14}$$

The high-frequency asymptotic derivation is based on the assumption that the length-scale of the heterogeneity is much greater than the length-scale across the high-frequency component of the fluid front. Stated another way, the high-frequency component of the pressure pulse, or of a jump in head, is assumed to be very sharp in comparison to the spatial variation in medium properties such as $\mathbf{K}(\mathbf{x})$ and $\zeta(\mathbf{x})$. Note that this assumption does break down at interfaces and in the presence of layering. But in such cases one can include the boundaries explicitly as boundary conditions, extending the reach of the algorithm at the cost of introducing considerably more complexity.

Returning to equation (14), if we assume that $\mathbf{K}$ only varies smoothly and correspondingly, the phase S also varies smoothly, then we can neglect the divergence of $\mathbf{K}\cdot\nabla S$ on the right-hand side of this equation. Therefore, equation (14) reduces to a form of the eikonal equation:

$$\frac{\partial S}{\partial t}+\nabla S\cdot\frac{\mathbf{K}}{\zeta}\cdot\nabla S=0. \tag{15}$$

For a comparison with the previous results of Vasco et al. (2000), consider a scalar hydraulic conductivity K in equation (15):

$$\nabla S\cdot\nabla S+\frac{\zeta}{K}\frac{\partial S}{\partial t}=0, \tag{16}$$

an eikonal equation similar to that of Vasco et al. (2000) and Fujita et al. (2015). The presence of the time derivative of S is due to the fact that we are still in the time domain and have not applied the Fourier transform. One can apply the method of characteristics to this scalar, first-order, partial differential equation (Courant & Hilbert, 1962) to derive a coupled set of ordinary differential equations for the trajectory $\mathbf{x}$ and the slowness gradient $\mathbf{p}$. These equations, derived in Vasco et al. (2000), are given by

$$\frac{d\mathbf{x}}{dt}=\mathbf{p}, \tag{17}$$

$$\frac{d\mathbf{p}}{dt}=\nabla\left[\frac{\zeta}{K}\right] \tag{18}$$

and we repeat them here for completeness, and because they will help us understand some of the examples presented below. It is also possible to solve equation (15) directly using numerical techniques such as a Fast Marching method (Sethian, 1999, p. 86) or methods for Hamilton-Jacobi equations such as level set methods (Osher & Fedkiw, 2003, p. 47). Such methods can be extremely efficient, allowing for the solution of large problems (Fujita et al., 2015; Zhang et al., 2014). The trajectories may also be determined in a hybrid fashion, by solving the eikonal equation numerically for $S(\mathbf{x},t)$ and then using equation (17) to find the trajectory $\mathbf{x}(t)$. The important point is that equations (17) and (18), defining the trajectories under the assumption of high-frequency propagation or smoothly varying properties, only depend on $\mathbf{K}$ and ζ and do not depend on the head field $h(\mathbf{x},t)$. That is, for a medium with sufficiently smooth properties, the amplitude of the pressure field decouples from the equation for the phase.

3. Applications

In this section, we compare the extended trajectories, calculated using equation (10), with the conventional high-frequency asymptotic trajectories that follow from the eikonal equation (16) or from the equivalent

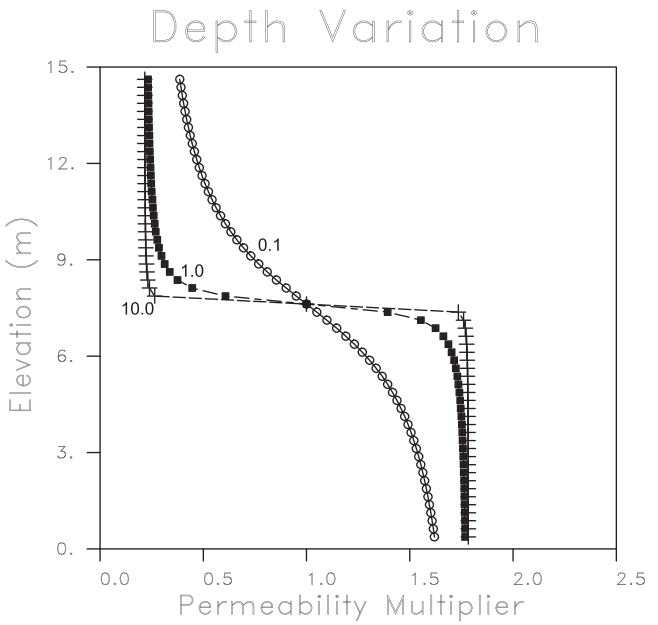

Figure 4. Depth variation of the permeability multipliers used in the three transition zone examples. The multipliers scale the permeability as a function of depth z, so that $\mathbf{K}(z)=\mu(z)\mathbf{K}_o$ where $\mathbf{K}_o$ is the background value. The scale factor varies with depth as $\mu(z)=1-\frac{1}{2}\arctan[\sigma(z-z_i)]$ where z_i is the location of the boundary and σ is a parameter controlling the width of the transition zone. Each curve is labeled by its respective parameter σ.

ordinary differential equations (17) and (18). We consider two cases that are commonly encountered, an interface of varying sharpness and a layer containing sharp boundaries. We also compare the compatibility of the two approaches with numerical model parameter sensitivity estimates.

3.1. First Illustration: A Single Interface

Perhaps the greatest challenge for high-frequency asymptotic methods are the sharp boundaries associated with interfaces, layering, and fracture zones. Such structures violate the assumption that the length scale of the heterogeneity is large in comparison with the length scale of the pressure front. While interfaces can be dealt with as explicit boundary conditions, such an approach is not usually helpful when solving inverse problems and attempting to image flow properties. When solving the inverse problem one does not typically know the locations of all sharp interfaces and high permeability features such as fracture zones.

In this section, we compare trajectories computed using a conventional high-frequency approach based on the eikonal equation (16) with those calculated using our proposed approach based on equation (10). We begin by considering a single interface of varying degrees of sharpness, as shown in Figure 4. The permeability is given by $\mathbf{K}(z)=\mu(z)\mathbf{K}_o$, where $\mu(z)$ is a scaling factor and $\mathbf{K}_o$ is the background permeability. The depth variation in the permeability modifier $\mu(z)$ is characterized by the function:

$$\mu(z)=1-\frac{1}{2}\arctan[\sigma(z-z_i)], \tag{19}$$

where σ is a parameter signifying the abruptness of the boundary, larger values of σ correspond to sharper interfaces. The position of the interface is specified by the parameter z_i, which in these examples is near 7.5 m in elevation.

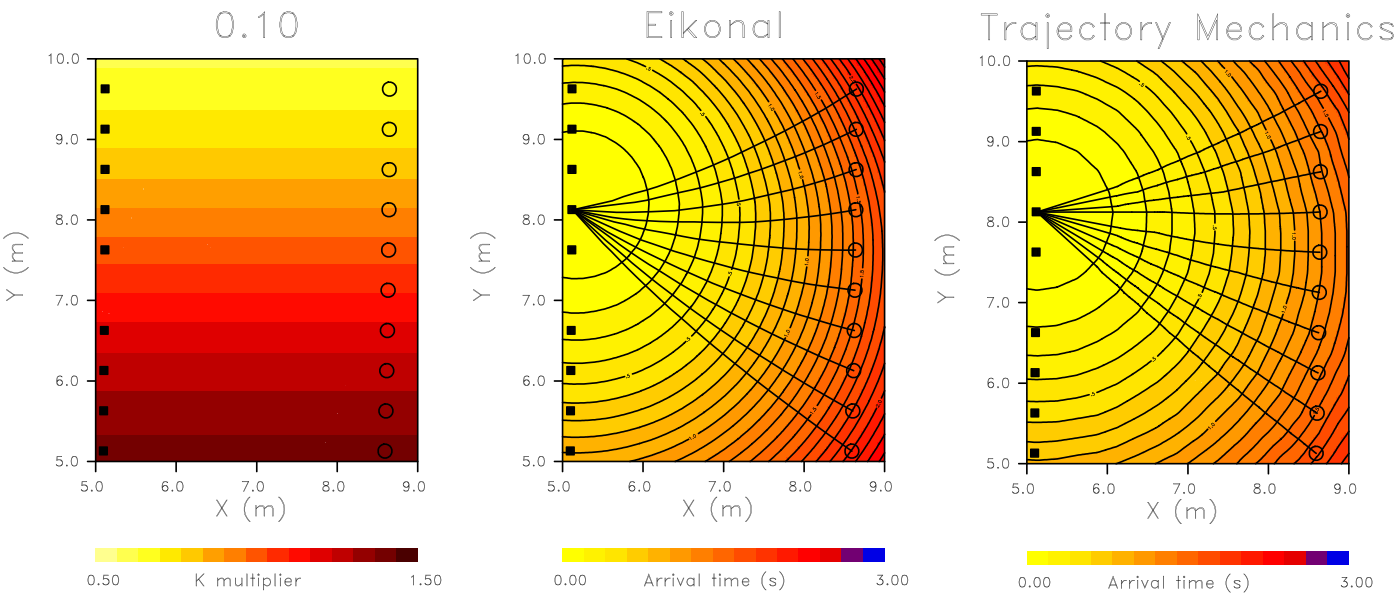

Figure 5. The first transition zone example, where $\sigma=0.1$, the smoothest variation. (left) The spatial variation of the permeability multiplier. The filled squares signify the locations of pressure sources. The open circles denote observations points. (middle) Trajectories calculated from a solution of the eikonal equation (16). (right) Extended trajectories obtained by solving equation (10), where $h(\mathbf{x},t)$ is calculated using the numerical simulator TOUGH2 (Pruess et al., 1999). The color scale indicates the variation of the travel time field that is computed directly from the numerical simulation, by extracting the time associated with the most rapid variation in pressure.

The smoothest interface considered, when $\sigma=0.1$, does not display any sharp discontinuities (see Figures 4 and 5). First, consider the high-frequency asymptotic solution obtained by solving the eikonal equation. We adopted the numerical solver proposed by Podvin and Lecomte (1991) for calculating the phase $S_{eikonal}$. The trajectories $\mathbf{x}(t)$ are found by solving

$$\frac{d\mathbf{x}}{dt}=\nabla S_{eikonal} \tag{20}$$

using an improved Euler's method known as Heun's or Ralston's method (Ascher & Petzold, 1998). The travel time field from the eikonal equation and the high-frequency trajectories are shown in Figure 5. The trajectories follow the gradient of the phase function from the eikonal equation, as indicated in equation (20).

Next, we implemented the extended trajectory mechanics approach to compute the paths. The numerical simulator TOUGH2 (Pruess et al., 1999) was used to calculate the evolution of the transient pressure and hydraulic head due to injection at the specified source. It is evident from equation (10) that the extended trajectories depend on the flow properties of the medium, in particular $\mathbf{K}$ and ζ, as well as the variation in the logarithm of the head $h(\mathbf{x},t)$. In Figure 5, we also plot the travel time field for a transient disturbance, calculated using the results from a TOUGH2 numerical simulation. Specifically, we use the transient pressure variation in each grid block, and its temporal derivative, to determine the time at which the pressure is changing most rapidly, as described in Vasco et al. (2000). In the examples, we will be neglecting the effects of gravity. For this case, in which the properties of the medium are smoothly varying, the trajectories derived using the eikonal equation and the trajectory mechanics approach are generally similar.

Now consider a transition in which the scale parameter σ for the sharpness of the boundary is an order of magnitude larger, taking a value of 1.0. This results in a notable interface (see Figures 4 and 6) and an abrupt change from a permeability multiplier of 0.2 to one approaching 1.75. We now observe differences in the trajectories computed using the high-frequency asymptotic approximation, based on the eikonal equation (equations (16) and (20)), and those computed using equation (10). The high-frequency trajectories bend strongly into the higher permeability half-space, following the strong changes in the phase function $S_{eikonal}$. The extended trajectory mechanics paths do bend somewhat due to the interface, but those for the upper four observation points stay above the sharp transition zone. The differences are due to the fact

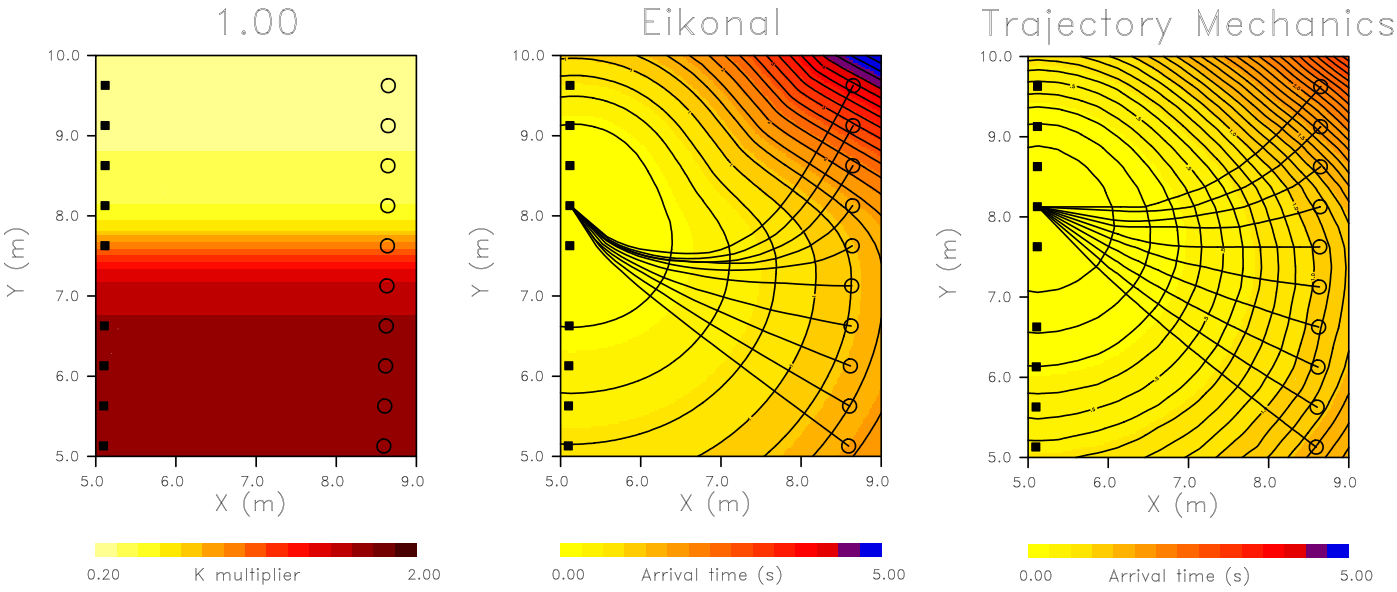

Figure 6. An example of a moderately sharp transition zone, where $\sigma=1.0$. (left) The spatial distribution of permeability used in the example. (middle) Trajectories resulting from the ordinary differential equation (20), where $S_{eikonal}$ is the solution of the eikonal equation. The color scale and contours represent variations in the travel time. (right) Trajectories that follow from conducting a reservoir simulation and then solving equation (10) using the head variation from the TOUGH2 simulator.

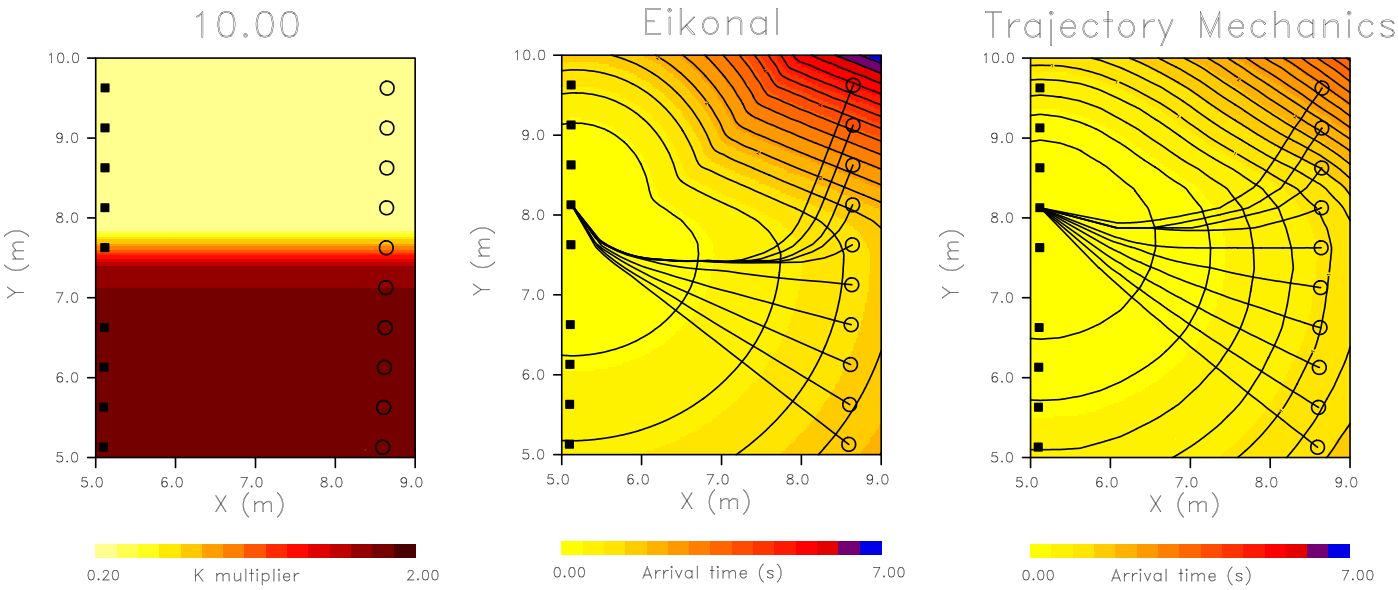

Figure 7. The sharpest transition zone with $\sigma = 10.0$, similar to an interface. (left) Variation in permeability. (middle) Trajectories calculated using the eikonal equation. The contour lines represent the distribution of arrival times produced by the eikonal equation. (right) Extended trajectories that are the solutions of equation (10). The travel time variation calculated using the numerical simulator is indicated by the color scale.

that the eikonal equation only accounts for the kinematics of the head propagation, which are controlled by **K** and ζ, and does not account for variations in head amplitude $h(\mathbf{x}, t)$.

Increasing the sharpness parameter σ by still another order of magnitude, to a value of 10.0, produces a transition that truly resembles a boundary (see Figures 4 and 7). The depth variation is similar to the previous case though the rounded corners of the transition are replaced with an abrupt jump. As before, the trajectories based on the eikonal equation bend sharply into the higher permeability half-space. The four uppermost trajectories appear to merge into a narrow pathway passing just below the interface and then bend sharply upward to their respective observation locations. These curves are determined by the phase field obtained from the eikonal equation and the paths proceed down the gradient of $S_{eikonal}$ to the source. Such paths minimize the travel time from the source to the receivers but ignore the coupling between the head amplitude field and the slowness field that comes into play when the heterogeneity varies rapidly in space. The extended trajectories are similar to those of the previous example, but the four uppermost paths do bend more due to the strong vertical variation in permeability. As before, these paths remain in the uppermost low permeability half-space, governed by the distribution of the logarithm of the head field.

3.2. Second Illustration: Layering

One might consider layering as simply the superposition of two interfaces, the upper and lower boundaries of the layer. However, the thickness of the layer introduces another length scale and thin layers might be expected to further violate any smoothness assumptions. In the example shown in Figure 8, we consider a layer roughly one meter in thickness, with almost an order of magnitude variation in permeability. The high-frequency trajectories, shown in the left of Figure 9, tend to propagate within the high permeability layer. The sole exceptions are two paths associated with observation points that are so far above the layer that they do not seem to be influenced by it. Note the strong distortion of the phase field within the layer and the kink in the phase field in the region above the layer. The extended trajectories, obtained by solving equation (10), all bend in response to the high permeability layer. The lowermost set of paths, those that cross the layer, are bent the most strongly, demonstrating the refraction that such sharp variations produce. The travel time field calculated from the output of the TOUGH2 numerical simulator appears to vary smoothly over the region and does not display the kink seen in the eikonal phase field.

While an order of magnitude permeability contrast is sufficient to illustrate the differences between the asymptotic and trajectory mechanics approaches, much larger variations can be expected in the subsurface. In order to visualize the effects of larger contrasts, let us consider layers that have permeabilities that are

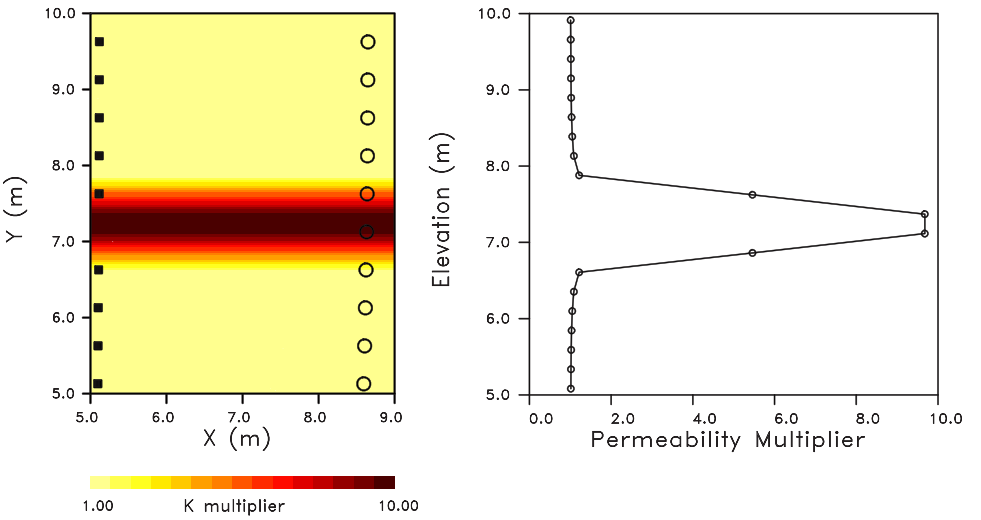

Figure 8. (left) Spatial variation in permeability used to represent a layer with sharp boundaries. (right) Depth variation of the permeability multiplier used to generate the layer.

100 and a 1,000 times greater than the background. When the permeability of the layer is two orders of magnitude greater than the background, all of the trajectories computed using the eikonal equation travel through its center (Figure 10). The extended trajectory mechanics paths are distributed above the layer, near the top of the layer, in the center of the layer, and at the base of the layer. The paths appear to be orthogonal to the contours of the simulator-based travel times, indicating propagation down the gradient of the travel time field. For a permeability contrast of 1,000, the trajectories calculated using the eikonal equation (Figure 11) do not differ much from the previous example. The trajectory mechanics paths are also very similar to those in Figure 10. For example, they are again perpendicular to the contours of the travel time field derived from the output of the reservoir simulator. The uppermost paths do appear to

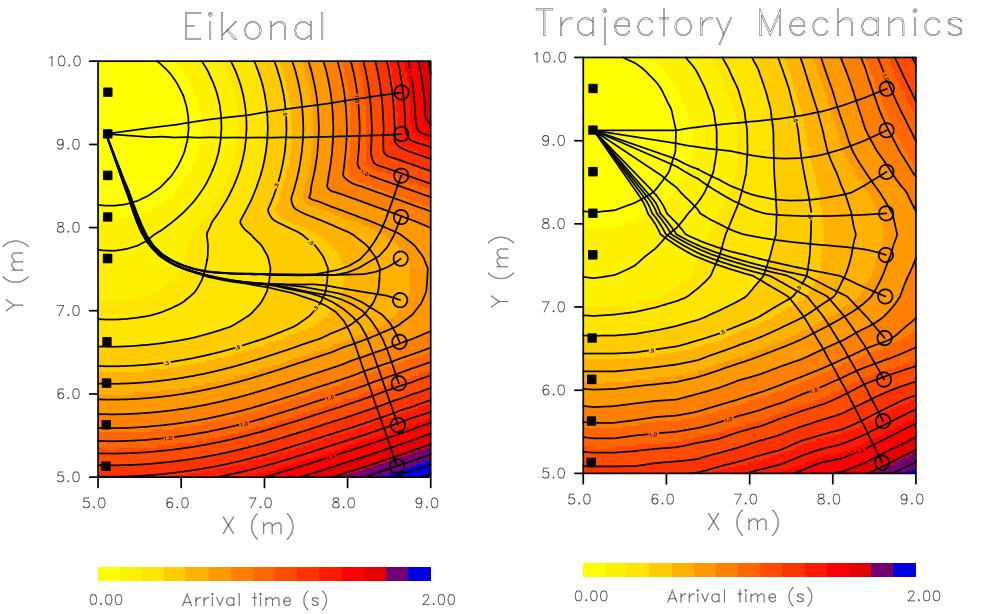

Figure 9. (left) Travel time contours derived from a solution of the eikonal equation. The trajectories resulting from the solution of equation (20) are also shown. (right) Extended trajectories determined by equation (10). These paths are controlled by both the permeability distribution and the logarithm of the pressure or head field. The trajectories are plotted on top of the arrival time field calculated using the output of the TOUGH2 numerical simulator.

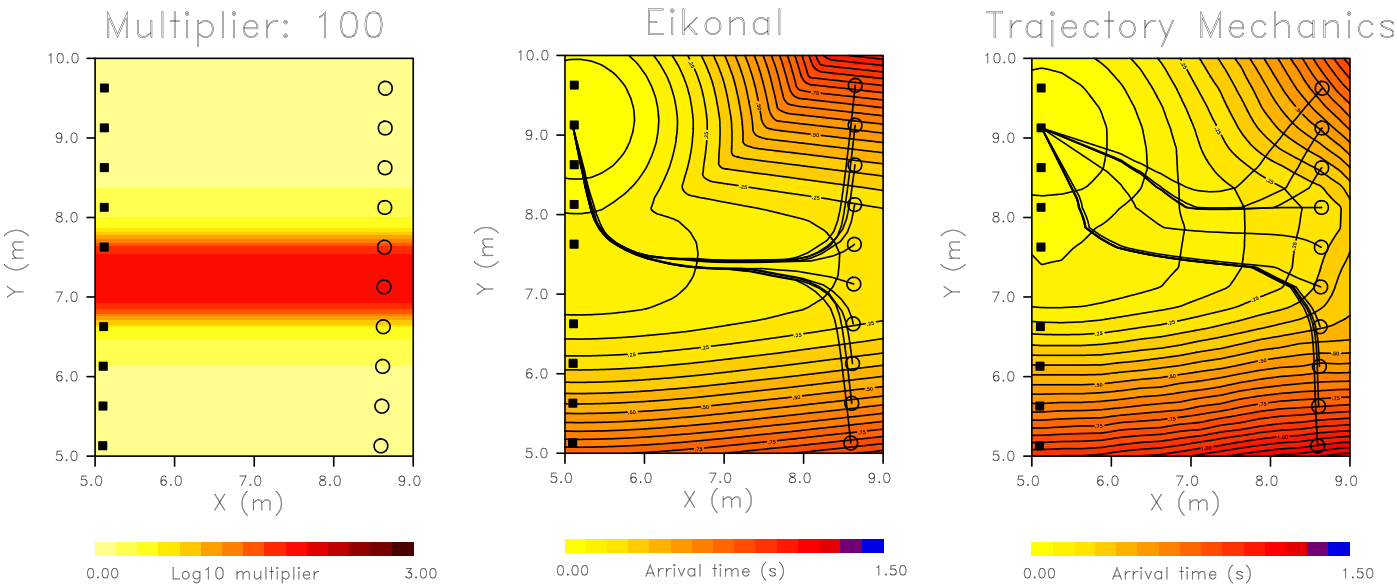

Figure 10. (left) An example of a sharp layer with a permeability 100 times greater than the background value. (middle) Trajectories resulting from the ordinary differential equation (20), where $S_{eikonal}$ is the solution of the eikonal equation. The color scale and contours represent variations in the travel time. (right) Trajectories that follow from conducting a reservoir simulation and then solving equation (10) using the head variation from the simulator. The arrival time field, computed from the numerical simulation results, is plotted as background color and contour variations.

concentrate near the top of the layer, well above those produced by the eikonal equation. Thus, when the permeability contrast is large enough the paths calculated by equation (10) bend significantly toward the layer.

3.3. Implications for Model Parameter Sensitivity Calculations

The differences in the paths calculated by the asymptotic approach and the method described here has implications for trajectory-based pressure tomography and the solution of the inverse problem. For

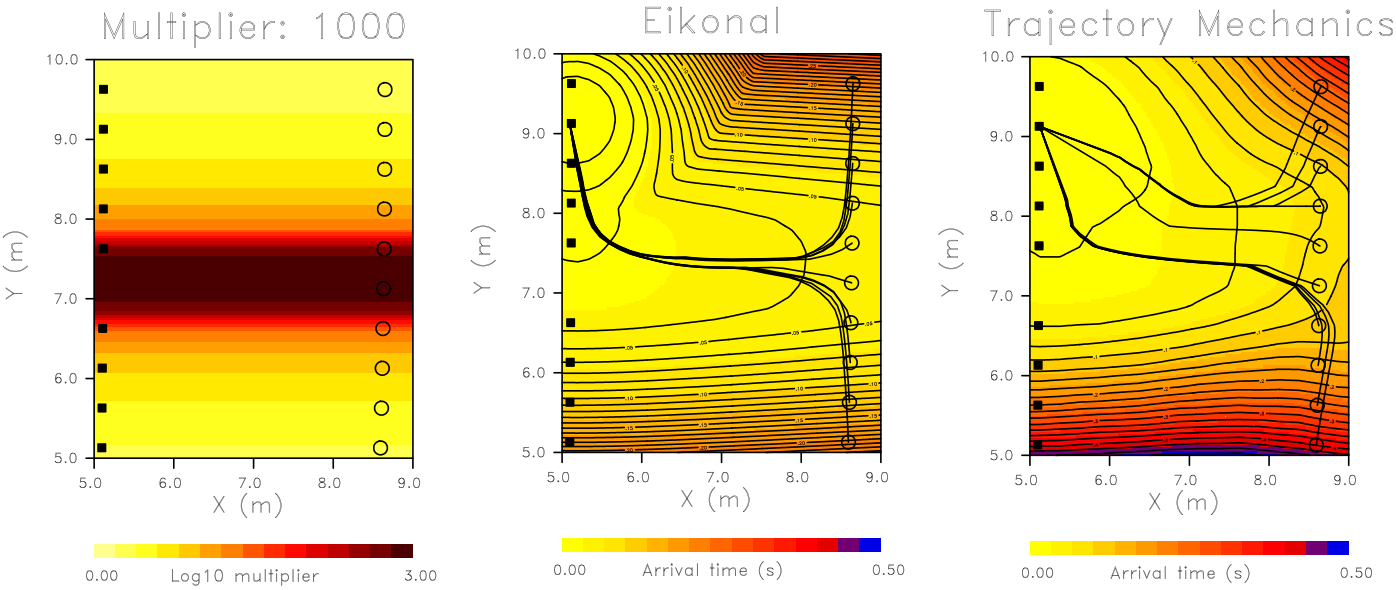

Figure 11. (left) An example of a sharp layer with a permeability 1,000 times greater than the background value. (middle) Trajectories resulting from the ordinary differential equation (20), where $S_{eikonal}$ is the solution of the eikonal equation. The color scale and contours represent variations in the travel time. (right) Trajectories that follow from conducting a reservoir simulation and then solving equation (10) using the head variation from the simulator. The arrival time field, computed from the numerical simulation results, is plotted as background color and contour variations.

example, iterative methods for updating reservoir models based on pressure travel time and waveform data rely on model parameter sensitivities to relate perturbations in reservoir properties to small changes in a calculated observable quantity (Carrera & Neuman, 1986; Jacquard & Jain, 1965; Oliver, 1993) Such sensitivities may be approximated using semianalytic, trajectory-based solutions leading to an efficient tomography-like solution to the inverse problem (Vasco et al., 2000). Let us consider how the presence of large and sharp permeability contrasts will perturb the trajectories calculated by the asymptotic and trajectory mechanics approaches, and how those trajectories compare with sensitivities obtained by a numerical perturbation technique.

Sensitivities are partial derivatives of an observed quantity with respect to changes in a specific model parameter. An observation may be a measurement of hydraulic head or pressure, or the arrival time of a transient disturbance. One may compute sensitivities using a numerical simulation code by simply perturbing the properties of a grid block, for example the grid block permeability, and calculating the resulting change in an observable quantity. Since we are interested in determining how rapid variations in flow properties alter the trajectories, our background model will consist of a sharp jump in permeability from 10 to 90 mdarcy (Figure 12). A step change in flow rate is used to generate a pressure transient that propagates from the source on the left, denoted by an open circle, to an observation point on the right (unfilled diamond). The time derivative of the pressure at the observation point is also plotted in Figure 12. Two measures of propagation time will be examined, the arrival time of the peak at the observation point, and an early time arrival, when the pressure exceeds 5% of the peak amplitude.

In order to get an idea of the spatial extent of the sensitivities and how that changes with time, we first compute sensitivities associated with pressure amplitudes. The numerical sensitivities are computed by perturbing the permeability in each of the grid blocks of the model and comparing the changes in observed pressure amplitudes. This requires $N + 1$ reservoir simulations where N is the number of grid blocks, in our case 962 simulator runs. The permeability sensitivities for an early time, 0.05 min after the start of injection, and a time corresponding to the peak in the rate of change, 3.4 min, are shown in Figure 13. The area of significant sensitivity generally broadens with time, as a larger region of the model can contribute to later pressure changes.

The travel time sensitivities are computed in a similar fashion, by perturbing the permeability in each grid block and calculating the changes in the travel time to the observation point. The permeability sensitivities for the early arrival time are plotted in Figure 14, along with the trajectories computed using the asymptotic approach, based on the eikonal equation, and the trajectory mechanics approach described here. The

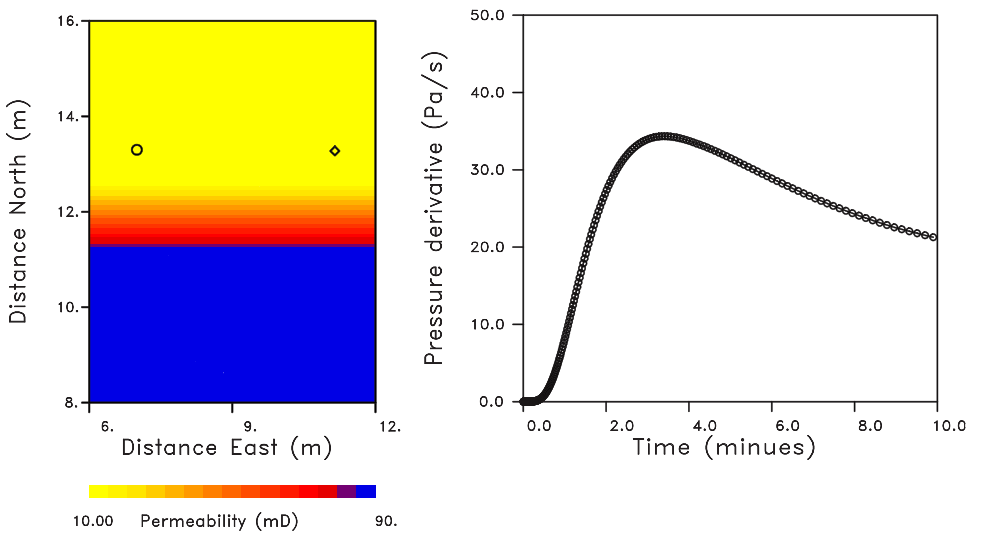

Figure 12. (left) Permeability model used in the sensitivity and trajectory calculations. A high permeability half-space of 90 mdarcy is adjacent to a region with a lower permeability of 10 mdarcy. The fluid injection site is denoted by an open circle. The observation point is indicated by an unfilled diamond. (right) The time derivative of the pressure trace calculated for the observation point.

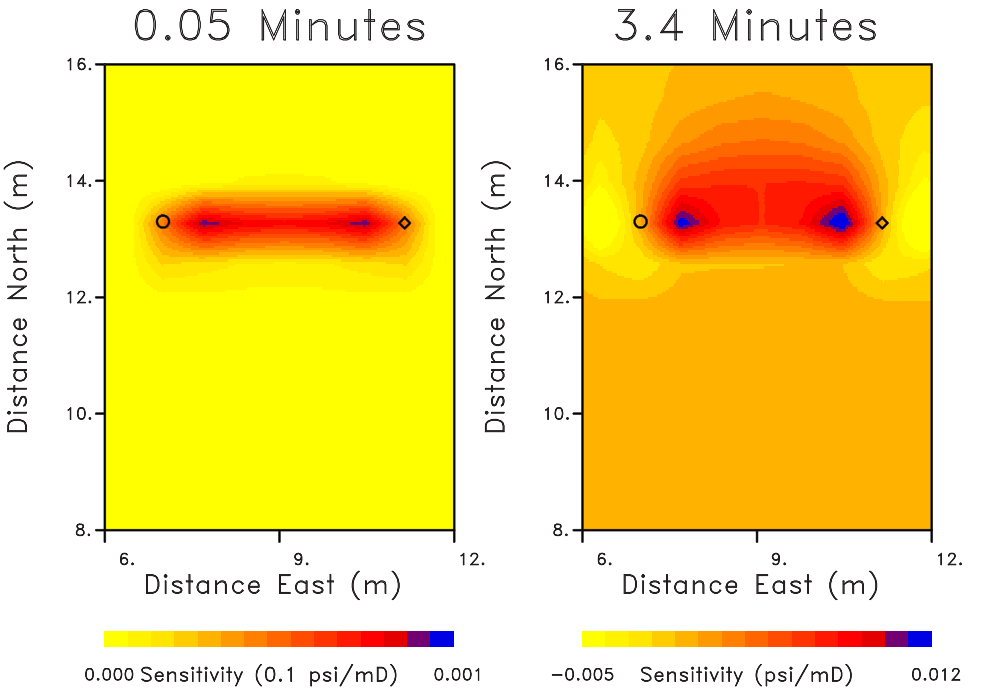

Figure 13. (left) Numerical pressure amplitude sensitivities calculated using a reservoir simulator and a perturbation technique. These sensitivities to permeability changes correspond to an early time of 0.05 min after the start of injection. (right) Numerical pressure amplitude sensitivities associated with the time at which the pressure is changing most rapidly (peak pressure time derivative in Figure 12), 3.4 min after the start of injection.

numerical sensitivities are concentrated in a narrow zone between the source and observation point, similar to the early time amplitude sensitivities in Figure 13. The trajectory produced by the solution to the eikonal equation deviates significantly from the area of peak permeability sensitivity. On the other hand, the path

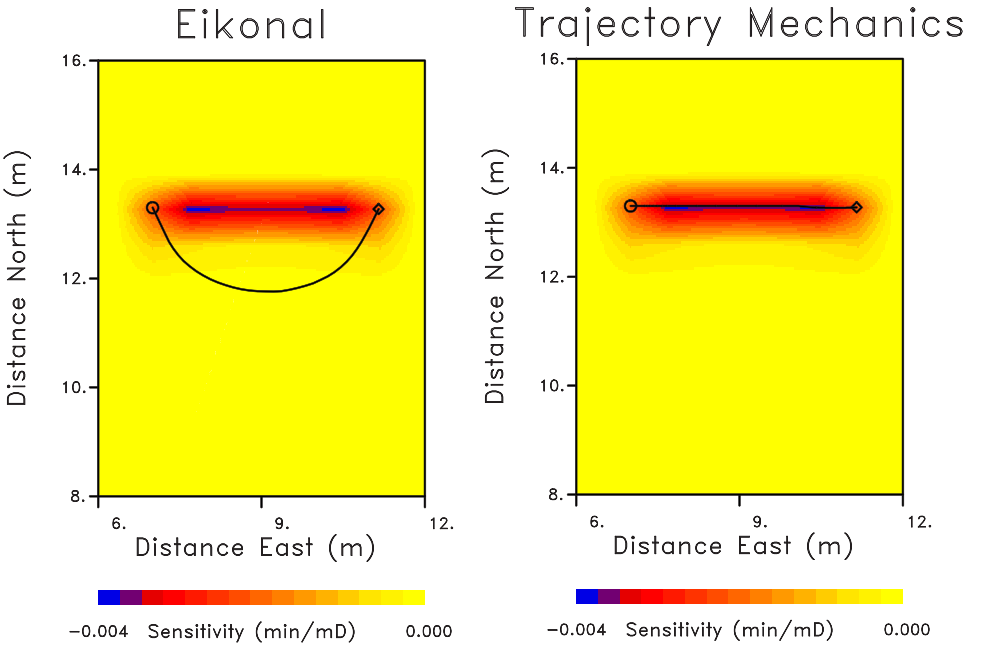

Figure 14. Pressure travel time sensitivities associated with an early time. (left) The trajectory computed using the eikonal equation following an asymptotic approximation. (right) The trajectory calculated using the trajectory mechanics approach is superimposed over the sensitivity values.

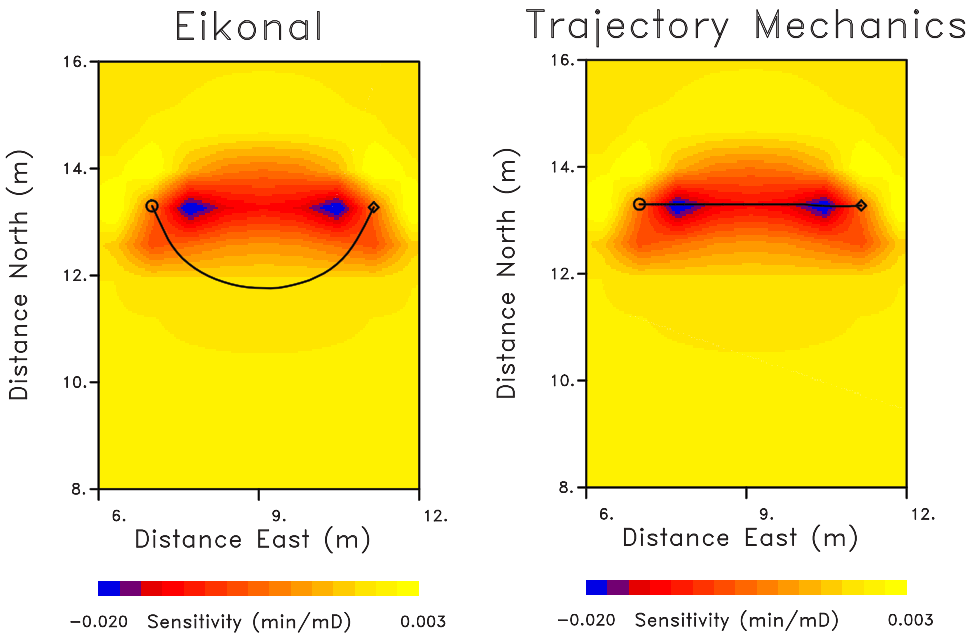

Figure 15. Pressure travel time sensitivities associated with the peak in Figure 12, when the pressure is changing most rapidly at the observation location. (left) The trajectory computed using the eikonal equation following an asymptotic approximation. (right) The trajectory calculated using the trajectory mechanics approach is superimposed over the sensitivity values.

computed by the trajectory mechanics approach follows the zone of peak sensitivity quite closely, traveling directly from the source to the observation point. The strong deviation in the asymptotic trajectory due to rapid variations in permeability was observed in the earlier illustrations of this section. This deviation reflects the breakdown of the assumption of a smoothly varying medium that is explicit in the asymptotic approach and techniques based on the eikonal equation.

Now consider the permeability sensitivities associated with the arrival time of the peak at the observation point, plotted in Figure 15. There is some asymmetry due to the presence of the high permeability below the source, but the peak sensitivity is still located in the region between the source and the observation location. Again, the trajectory based on the eikonal equation curves down toward the high permeability half-space and away from areas of high sensitivity. By contrast, the trajectory mechanics path, calculated using equation (10), traverses the area of greatest permeability sensitivity.

The actual computation of arrival time sensitivities is complicated by the coupling between the propagation time and the amplitude that is evident in equation (10). A direct perturbation of this expression, say with respect to a change in permeability, needs to account for the change in $h(\mathbf{x}, t)$ due to the perturbation in $\mathbf{K}$. Such an effect might be small, but given the fact that abrupt and large changes in permeability are allowed in the background model, one would need to verify this for a given model. An alternative approach, based on cross-correlation arrival times and the Born approximation, does account for the coupling between propagation time and amplitude (Luo & Schuster, 1991; Vasco & Majer, 1993). However, the technique is essentially an adjoint-state computation and requires two complete forward calculations, one from the source point and one from the observation point. Additional work will be required to determine the efficiency and accuracy of the various methods for approximating arrival time sensitivities.

4. Conclusions

Using the trajectory mechanics it is possible to retain a semianalytic formulation, similar to that used in an asymptotic approach, while extending the validity of the computed trajectories to media with arbitrary property variations. The price that one must pay for this is a numerical pressure calculation for each distinct pressure source. This can be done with any existing numerical simulator, the results are simply

postprocessed to extract the necessary quantities for calculating the trajectories. The trajectories may form the basis of an efficient inversion of pressure travel times for hydraulic diffusivity, akin to medical and geophysical tomography. The trajectories also provide insight on pressure propagation in highly heterogeneous media and allows for the visualization of the paths of pressure transients.

Because the approach requires a reservoir simulation for each source, the technique is more computationally intensive then a solution based solely on the eikonal equation. Similarly, the approach may require more computation then methods that reduce the transient pressure equation so a simpler form, such as moment-based methods (Li et al., 2005; Yin & Illman, 2009; Zhu & Yeh 2006) or the sinusoidal pumping tests (Bernabe et al., 2005; Black & Kipp, 1981; Cardiff et al., 2013b; Kuo, 1972; Rasmussen et al., 2003; Renner & Messar 2006). It may be possible to improve the efficiency through the use of simplified numerical simulators that are designed solely to calculate pressure, particularly when a single fluid phase is present. Or to modify the method to consider a periodic source and adopt the steady-periodic approach. Alternatively, it might be possible to adopt a hybrid approach in which the eikonal equation is used for the early iterations of an inversion, when the heterogeneity is rather smooth, and then to switch to the trajectory mechanics approach for the later iterations. In a companion paper we will consider the application of this technique to both synthetic and field transient pressure arrival times, addressing the computational questions in more detail.

High-frequency and multiscale asymptotic methods also provide efficient modeling techniques but they are based on the assumption of smoothly varying heterogeneity (Vasco, 2008; Vasco & Datta-Gupta, 2016; Vasco et al., 2000; Zhang et al., 2014). By comparing such an approach with an extended trajectory-based technique we find that, as predicted, the asymptotic method does indeed break down in the presence of rapid changes in material properties. Thus, trajectories resulting from solving the eikonal equation, the product of an asymptotic formulation, may deviate from the actual path of a transient pressure pulse. The deviations are particularly severe for thin layers, a fairly common occurence in the subsurface. It appears that the amplitude-phase coupling that is present in actual wavefields stabilizes the trajectories, at least in the case of the diffusion-like equation considered here. This has implications for the inverse problem, in which one is trying to image spatial variations in flow properties. As the estimated heterogeneity grows in magnitude and rapid spatial variations materialize, the high-frequency trajectories become increasingly inaccurate. As illustrated in the sensitivity calculations above, this may lead to incorrect model parameter sensitivities. In tomographic imaging, trajectories are used to compute approximate model parameter sensitivities (Brauchler et al., 2003; Fujita et al., 2015; Vasco et al., 2000). Therefore, the trajectories must reflect the main contribution to the model parameter sensitivities. If the trajectories are in error, as due to the breakdown of the eikonal equation in the presence of rapidly varying heterogeneity, then an iterative updating algorithm could put anomalies in incorrect locations.

Appendix A: Derivation of the Equations Defining the Trajectories

In this appendix, we derive the ordinary differential equations that determine the trajectories associated with a propagating disturbance. The approach is similar to a derivation of the eikonal equation (Vasco & Datta-Gupta, 2016) though we make no assumptions concerning the smoothness of the medium parameters $\mathbf{K}$ and ζ, allowing for arbitrary spatial distributions of properties. This results in a system of equations that is somewhat more complicated than those associated with a high-frequency asymptotic solution. However, with the aid of a numerical simulator we can solve for one set of variables and produce a direct equation for the trajectory.

Our derivation is based on the work of Garashchuk and Vazhappilly (2010) for the time-dependent Schrödinger equation in imaginary time, a form of the diffusion equation. We start with the equation governing the evolution of hydraulic head $h(\mathbf{x}, t)$, a function of spatial variables $\mathbf{x}$ and time t,

$$\nabla \cdot \mathbf{K} \cdot \nabla h = \zeta \frac{\partial h}{\partial t}, \tag{A1}$$

where $\mathbf{K}$ is a symmetric matrix (de Marsily, 1986). In order to derive equations for trajectories we substitute the expression:

$$h(\mathbf{x}, t) = e^{-S(\mathbf{x},t)} \tag{A2}$$

into the governing equation (A1). The derivatives in equation (A1) may be rewritten in terms of the new variable $S(\mathbf{x}, t)$, for example we have

$$\nabla h = -\nabla S e^{-S}. \tag{A3}$$

The modified spatial and temporal derivative terms may be used to write equation (A1) in terms of S:

$$\nabla \cdot (\mathbf{K} \cdot \nabla S) - \nabla S \cdot \mathbf{K} \cdot \nabla S = \zeta \frac{\partial S}{\partial t}, \tag{A4}$$

where we have factored out the exponential term in S, under the assumption that the pressure never vanishes nor does it become infinite. Defining the slowness vector, the spatial gradient of $S(\mathbf{x}, t)$:

$$\mathbf{p} = \nabla S \tag{A5}$$

allows us to write equation (A4) as

$$\zeta \frac{\partial S}{\partial t} + \mathbf{p} \cdot \mathbf{K} \cdot \mathbf{p} = \nabla \cdot (\mathbf{K} \cdot \mathbf{p}). \tag{A6}$$

Dividing through by ζ and defining

$$\Upsilon = \frac{\mathbf{K}}{\zeta} \tag{A7}$$

and

$$\mathbf{v} = \mathbf{p} \cdot \Upsilon \tag{A8}$$

allows us to write equation (A6) as

$$\frac{\partial S}{\partial t} + \mathbf{v} \cdot \nabla S = \frac{1}{\zeta} \nabla \cdot (\mathbf{K} \cdot \mathbf{p}). \tag{A9}$$

Considering the equation in a Lagrangian reference frame moving with velocity $\mathbf{v}$, we can define the total time derivative of S:

$$\frac{dS}{dt} = \frac{\partial S}{\partial t} + \mathbf{v} \cdot \nabla S = \frac{\partial S}{\partial t} + \frac{d\mathbf{x}}{dt} \cdot \nabla S, \tag{A10}$$

where $\mathbf{x}(t)$ is the trajectory traced out as a function of time due to the velocity field $\mathbf{v}$. From the preceding equation we note that

$$\frac{d\mathbf{x}}{dt} = \mathbf{v} = \mathbf{p} \cdot \Upsilon \tag{A11}$$

provides an ordinary differential equation for the trajectory $\mathbf{x}(t)$. Writing this equation explicitly in terms of $\mathbf{K}$ and ζ gives

$$\frac{d\mathbf{x}}{dt} = \frac{1}{\zeta} \mathbf{p} \cdot \mathbf{K}. \tag{A12}$$

Writing equation (A9) in terms of the Lagrangian reference frame produces an ordinary differential equation for $S(\mathbf{x}, t)$ along the trajectory:

$$\frac{dS}{dt} = \frac{1}{\zeta} \nabla \cdot (\mathbf{K} \cdot \mathbf{p}). \tag{A13}$$

In order to write this equation more succinctly, we define a variable $U(\mathbf{x}, t)$, representing the right-hand side

$$U(\mathbf{x}, t) = \frac{1}{\zeta} \nabla \cdot (\mathbf{K} \cdot \mathbf{p}) \tag{A14}$$

so that equation (A13) becomes

$$\frac{dS}{dt} = U. \tag{A15}$$

Applying the gradient operator to both sides of equation (A15) produces an ordinary differential equation for $\mathbf{p}$,

$$\frac{d\mathbf{p}}{dt} = \nabla U = \nabla\left[\frac{1}{\zeta}\nabla\cdot(\mathbf{K}\cdot\mathbf{p})\right]. \tag{A16}$$

Equations (A12) and (A16) define a coupled system of equations for the trajectory $\mathbf{x}(t)$ and $\mathbf{p}$. Specifically, the trajectory associated with a propagating pressure disturbance may be found by solving the coupled system of ordinary differential equations

$$\frac{d\mathbf{x}}{dt} = \frac{1}{\zeta}\mathbf{p}\cdot\mathbf{K},$$

$$\frac{d\mathbf{p}}{dt} = \nabla\left[\frac{1}{\zeta}\nabla\cdot(\mathbf{K}\cdot\mathbf{p})\right].$$

Unsing numerical methods, one can solve these equation for the trajectory and the phase gradient (Press et al., 1992; Wyatt, 2005). This is the approach taken in quantum mechanics to compute trajectories associated with Schrödinger's wave equation (Garashchuk, 2010; Garashchuk et al., 2011; Wyatt, 2005). However, due to the presence of gradient operators in these ordinary differential equations, the numerical solution of the coupled equations require involved algorithms in which the trajectories are coupled. The approach is still very efficient in comparison to a fully numerical, grid-based solution of Schrödinger's wave equation and has led to practical quantum mechanical calculations for complicated chemical systems (Wyatt, 2005).

Alternatively, one can use the results of a numerical simulator, such as TOUGH2 (Pruess et al., 1999) to calculate the trajectories. We can go back to the definition of $S(\mathbf{x},t)$, given by equation (A2), to write it in terms of the hydraulic head:

$$S(\mathbf{x},t) = -\ln h(\mathbf{x},t) \tag{A17}$$

and to calculate $\mathbf{p}=\nabla S$. Therefore, we can write the equation for the trajectory $\mathbf{x}(t)$ directly in terms of the hydraulic head:

$$\frac{d\mathbf{x}}{dt} = -\frac{\mathbf{K}}{\zeta}\cdot\nabla\ln h. \tag{A18}$$

Then the two equations (A12) and (A16) uncoupled and one only has to solve equation (A18) for the trajectory. Alternatively, by taking advantage of existing numerical simulators, we can use the calculated values of $h(\mathbf{x},t)$ to determine $S(\mathbf{x},t)$ and $\mathbf{p}$. In taking this approach, we lose some of the efficiency that is associated with solving the system of ordinary differential equations or the related eikonal equation. However, we gain significantly in the range of applicability of our trajectory calculations. Furthermore, we still maintain the trajectory-based formalism for tomographic inversion and all the efficiencies that are associated with this approach to imaging. Finally, the trajectory calculations are no longer coupled and we can compute the paths one at a time, which also allows for simple parallelization if necessary.

Acknowledgments

Work performed at Lawrence Berkeley National Laboratory was supported by the US Department of Energy under contract DE-AC02-05-CH11231, Office of Basic Energy Sciences of the US Department of Energy. The main contributions of this work are the expressions for the extended trajectories, no new data or models are presented in this paper. The pressure fields were computed using the iTough2 package that is available through Lawrence Berkeley National Laboratory, see esd1.lbl.gov/research/projects/tough/licensing/itough2.html.

References

Ascher, U. M., & Petzold, L. R. (1998). *Computer methods for ordinary differential equations and differential-algebraic equations*. Philadelphia, PA: Society for Industrial and Applied Mathematics.

Bernabe, Y., Mok, U., & Evans, B. (2005). A note on the oscillating flow method for measuring rock permeability. *International Journal of Rock Mechanics and Mining Science*, *43*, 311–316.

Black, J. H., & Kipp, K. L. (1981). Determination of hydrogeological parameters using sinusoidal pressure tests: A theoretical appraisal. *Water Resources Research*, *17*, 686–692.

Bohling, G. C., Zhan, X., Butler, J. J., & Zheng, L. (2002). Steady shape analysis of tomographic pumping tests for characterization of aquifer heterogeneities. *Water Resources Research*, *38*(12), 1324. https://doi.org/10.1029/2001WR001176

Brauchler, R., Hu, R., Dietrich, P., & Sauter, M. (2011). A field assessment of high-resolution aquifer characterization based on hydraulic travel time and hydraulic attenuation tomography. *Water Resources Research*, *47*, W03503. https://doi.org/10.1029/2010WR009635

Brauchler, R., Hu, R., Vogt, T., Al-Halbouni, D., Heinrichs, T., Ptak, T., et al. (2010). Cross-well slug interference tests: An effective characterization method for resolving aquifer heterogeneity. *Journal of Hydrology*, *384*, 33–45.

Brauchler, R., Liedl, R., & Dietrich, P. (2003). A travel time based hydraulic tomographic approach. *Water Resources Research*, *39*(12), 1370. https://doi.org/10.1029/2003WR002262

Butler, J. J., Garnett, E. J., & Healey, J. M. (2003). Analysis of slug tests in formations of high hydraulic conductivity. *Ground Water*, *41*, 620–630.

Butler, J. J., McElwee, C. D., & Bohling, G. C. (1999). Pumping tests in networks of multilevel sampling wells: Motivation and methodology. *Water Resources Research*, *35*, 3553–3560.

Cardiff, M., Bakhos, T., Kitanidis, P. K., & Barrash, W. (2013b). Aquifer heterogeneity characterization with oscillatory pumping: Sensitivity analysis and imaging potential. *Water Resources Research*, *49*, 5395–5410. https://doi.org/10.1002/wrcr.20356

Cardiff, M., & Barrash, W. (2011). 3-D transient hydraulic tomography in unconfined aquifers with fast drainage response. *Water Resources Research*, *47*, W12518. https://doi.org/10.1029/2010WR010367

Cardiff, M., Barrash, W., & Kitanidis, P. K. (2013a). Hydraulic conductivity imaging from 3-D transient hydraulic tomography at several pumping/observation densities. *Water Resources Research*, *49*, 7311–7326. https://doi.org/10.1002/wrcr.20519
Carrera, J., & Neuman, S. P. (1986). Estimation of aquifer parameters under transient and steady state conditions: 1. Maximum likelihood method incorporating prior information. *Water Resources Research*, *22*, 199–210.
Cash, J. R., & Carp, A. H. (1990). A variable order Runge-Kutta method for initial value problems with rapidly varying right-hand sides. *ACM Transactions on Mathematical Software*, *16*, 201–222.
Chapman, C. H. (2004). *Fundamentals of seismic wave propagation*. Cambridge, UK: Cambridge University Press.
Cheng, H., He, Z., & Datta-Gupta, A. (2005). A comparison of travel-time and amplitude matching for field-scale production data integration: Sensitivity, non-linearity, and practical implications. *Society of Petroleum Engineering Journal*, *10*, 75–90.
Cohen, J. K., & Lewis, R. M. (1967). A ray method for the asymptotic solution of the diffusion equation. *Journal of the Institute for Mathematics and Its Applications*, *3*, 266–290.
Courant, R., & Hilbert, D. (1962). *Methods of mathematical physics*. New York, NY: John Wiley.
de Marsily, G. (1986). *Quantitative hydrogeology*. San Diego, CA: Academic.
Fujita, Y., Datta-Gupta, A., & King, M. J. (2015). A comprehensive reservoir simulator for unconventional reservoirs that is based on the Fast Marching method and diffusive time of flight. *SPE Journal*, *21*, 2276–2288. https://doi.org/10.2118/173269-PA
Garashchuk, S. (2010). Quantum trajectory dynamics in imaginary time with the momentum-dependent quantum potential. *Journal of Chemical Physics*, *132*, 014112. https://doi.org/10.1063/1.3289728
Garashchuk, S., Mazzuca, J., & Vazhappilly, T. (2011). Efficient quantum trajectory representation of wavefunctions evolving in imaginary time. *Journal of Chemical Physics*, *135*, 034104. https://doi.org/10.1063/1.3610165
Garashchuk, S., & Vazhappilly, T. (2010). Multidimensional quantum trajectory dynamics in imaginary time with approximate quantum potential. *Journal of Physical Chemistry*, *114*, 20595–20602. https://doi.org/10.1021/jp1050244
Goldfarb, Y., Degani, I., & Tannor, D. J. (2006). Bohmian mechanics with complex action: A new trajectory-based formulation for quantum mechanics. *Journal of Chemical Physics*, *125*, 231103.
He, Z., Datta-Gupta, A., & Vasco, D. W. (2006). Rapid inverse modeling of pressure interference tests using trajectory-based traveltime and amplitude sensitivities. *Water Resources Research*, *42*, W03419. https://doi.org/10.1029/2004WR003783
Hsieh, P. A., Neuman, S. P., Stiles, G. K., & Simpson, E. S. (1985). Field determination of the three-dimensional hydraulic conductivity tensor of anisotropic media: 2. Methodology and application to fractured rocks. *Water Resources Research*, *21*, 1667–1676.
Hu, R., Brauchler, R., Herold, M., & Bayer, P. (2011). Hydraulic tomography analog outcrop study: Combining travel time and steady shape inversion. *Journal of Hydrology*, *409*, 350–362.
Jacquard, P., & Jain, C. (1965). Permeability distribution from field pressure data. *Society of Petroleum Engineering Journal*, *5*, 281–294.
Karasaki, K., Freifeld, B., Cohen, A., Grossenbacher, K., Cook, P., & Vasco, D. (2000). A multidisciplinary fractured rock characterization study at the Raymond field site, Raymond California. *Journal of Hydrology*, *236*, 17–34.
Kline, M., & Kay, I. W. (1965). *Electromagnetics theory and geometrical optics*. New York, NY: Interscience.
Kuo, C. (1972). Determination of reservoir properties from sinusoidal and multirate flow tests in one or more wells. *Society of Petroleum Engineering Journal*, *12*, 499–507.
Li, W., Nowak, W., & Cirpka, O. A. (2005). Geostatistical inverse modeling of transient pumping tests using temporal moments of drawdown. *Water Resources Research*, *41*, W08403. https://doi.org/10.1029/2004WR003874
Liu, J., & Makri, N. (2005). Bohm's formulation in imaginary time: Estimation of energy eigenvalues. *Molecular Physics*, *103*, 1083–1090. https://doi.org/10.1080/00268970512331339387
Luneburg, R. K. (1966). *Mathematical theory of optics*. Berkeley, CA: University of California Press.
Luo, Y., & Schuster, G. T. (1991). Wave-equation traveltime inversion. *Geophysics*, *56*, 645–653. https://doi.org/10.1190/1.1443081
Oliver, D. W. (1993). The influence of nonuniform transmission and storativity on drawdown. *Water Resources Research*, *29*, 169–178.
Osher, S., & Fedkiw, R. (2003). *Level set methods and dynamic implicit surfaces*. New York, NY: Springer.
Paillet, F. L. (1993). Using borehole geophysics and cross-borehole flow testing to define connections between fracture zones in bedrock aquifers. *Journal of Applied Geophysics*, *30*, 261–279.
Podvin, P., & Lecomte, I. (1991). Finite-difference computation of traveltimes in very contrasted velocity models: A massively parallel approach and its associated tools. *Geophysical Journal International*, *105*, 271–284.
Press, W. H., Teukolsky, S. A., Vetterling, W. T., & Flannery, B. P. (1992). *Numerical recipes*. Cambridge, UK: Cambridge University Press.
Pruess, K., Oldenburg, C., & Moridis, G. (1999). *TOUGH2 user's guide, version 2.0* (LBNL Rep. 43134). Berkeley.
Rasmussen, T. C., Haborak, K. G., & Young, M. H. (2003). Estimating aquifer hydraulic properties using sinusoidal pumping at the Savannah River Site, South Carolina, USA. *Hydrogeological Journal*, *11*, 466–482.
Renner, J., & Messar, M. (2006). Periodic pumping tests. *Geophysical Journal International*, *167*, 479–493.
Rucci, A., Vasco, D. W., & Novali, F. (2010). Fluid pressure arrival-time tomography: Estimation and assessment in the presence of inequality constraints with an application to production at the Krechba field, Algeria. *Geophysics*, *75*, O39–O55. https://doi.org/10.1190/1.3493504
Sethian, J. A. (1999). *Level set methods and Fast Marching methods*. Cambridge, UK: Cambridge University Press.
Vasco, D. W. (2004). Estimation of flow properties using surface deformation and head data: A trajectory-based approach. *Water Resources Research*, *40*, W10104. https://doi.org/10.1029/2004WR003272
Vasco, D. W. (2008). Zeroth-order inversion of transient pressure observations. *Inverse Problems*, *24*, 1–21. https://doi.org/10.1088/0266-5611/24/2/025013
Vasco, D. W., Daley, T. M., & Bakulin, A. (2014). Utilizing the onset of time-lapse changes: A robust basis for reservoir monitoring and characterization. *Geophysical Journal International*, *197*, 542–556. https://doi.org/10.1093/gji/ggt526
Vasco, D. W., & Datta-Gupta, A. (2016). *Subsurface fluid flow and imaging*. Cambridge, UK: Cambridge University Press.
Vasco, D. W., & Karasaki, K. (2001). Inversion of pressure observations: An integral formulation. *Journal of Hydrology*, *253*, 27–40.
Vasco, D. W., Keers, H., & Karasaki, K. (2000). Estimation of reservoir properties using transient pressure data: An asymptotic approach. *Water Resources Research*, *36*, 3447–3465.
Vasco, D. W., & Majer, E. L. (1993). Wavepath traveltime tomography. *Geophysical Journal International*, *115*, 1055–1069. https://doi.org/10.1111/j.1365-246X.1993.tb01509.x
Virieux, J., Flores-Luna, C., & Gibert, D. (1994). Asymptotic theory for diffusive electromagnetic imaging. *Geophysical Journal International*, *119*, 857–868.
Wyatt, R. E. (2005). *Quantum dynamics with trajectories*. New York, NY: Springer.

Yeh, T.-C. J., Lee, C. H., Hsu, K. C., & Wen, J. C. (2008). Fusion of hydrologic and geophysical tomographic surveys. *Geosciences Journal*, *12*, 159–167.

Yeh, T.-C. J., & Liu, S. (2000). Hydraulic tomography: Development of a new aquifer test method. *Water Resources Research*, *36*, 2095–2105.

Yin, D., & Illman, W. (2009). Hydraulic tomography using temporal moments of drawdown recovery data: A laboratory sandbox study. *Water Resources Research*, *45*, W01502. https://doi.org/10.1029/2007WR006623

Zhang, Y., Bansal, N., Fujita, Y., Datta-Gupta, A., King, M. J., & Sankaran, S. (2014). From streamlines to Fast Marching: Rapid simulation and performance assessment of shale-gas reservoirs by use of diffusive time of flight as a spatial coordinate. *SPE Journal*, *21*, 1883–1898. https://doi.org/10.2118/168997-PA

Zhu, J., & Yeh, J. T.-C. (2006). Analysis of hydraulic tomography using temporal moments of drawdown recovery data. *Water Resources Research*, *42*, W02403. https://doi.org/10.1029/2005WR004309